

Measurement of $^{19}\text{F}(\gamma, \alpha)^{15}\text{N}$ with a bubble chamber and a bremsstrahlung beam

C. Ugalde ^{*†}

*The University of Chicago, Chicago, IL 60637 and Argonne National Laboratory,
Argonne IL 60439, USA*

B. DiGiovine, R. J. Holt[†],
A. El Alaoui, K. Hafidi, D. Henderson, K. E. Rehm

Argonne National Laboratory, Argonne IL 60439, USA

R. Suleiman [†], A. Freyberger, J. Grames, R. Kazimi
M. Poelker, R. Mammei, D. Meekins

Jefferson Lab, Newport News, VA 23606, USA

A. Sonnenschein

Fermi National Accelerator Laboratory, Batavia, IL 60510, USA

A. Robinson

The University of Chicago, Chicago, IL 60637, USA

A. E. Champagne

*Triangle Universities Nuclear Laboratory, Durham, NC 27708, USA and University of
North Carolina, Chapel Hill, NC 27599, USA*

N. Kalantarians

Hampton University, Hampton, VA 23668, USA

[†] Co-spokesperson

^{*} Contact: Claudio Ugalde (cugalde@anl.gov)

4 May 2012

Abstract

We have devised a new technique for determining thermonuclear reaction rates of astrophysical importance. By measuring (γ, α) cross sections we will determine (α, γ) reaction rates of processes such as $^{15}\text{N}(\alpha, \gamma)^{19}\text{F}$ and $^{12}\text{C}(\alpha, \gamma)^{16}\text{O}$ with a considerable improvement in sensitivity from previous experiments. Adopting ideas from dark matter search experiments with bubble detectors, we have found that a superheated liquid is sensitive to α -particle and heavy ion recoils produced from a γ ray beam impinging on the nuclei in the liquid. The main advantage of the new target-detector system is a density factor of 4-6 orders of magnitude higher than conventional gas targets. Also, the detector is virtually insensitive to the γ -ray beam itself, thus allowing us to detect only the products of the nuclear reaction of interest. This proposal requests 100 hours of beam time for measuring the $^{15}\text{N}(\alpha, \gamma)^{19}\text{F}$ reaction. With this new method data can be recorded directly in the Gamow window. Only one other case of this is known. Depending on the success of the experiment, we will submit a separate proposal for the measurement of the key astrophysical reaction $^{12}\text{C}(\alpha, \gamma)^{16}\text{O}$.

Contents

1	Introduction	4
1.1	The nucleosynthesis of fluorine	4
1.2	Fluorine production in AGB stars	4
1.3	Fluorine production in Wolf-Rayet stars	6
1.4	The current reaction rate of $^{15}\text{N}(\alpha, \gamma)^{19}\text{F}$	7
2	Method	8
3	Detector	12
4	Previous experiments	14
5	Backgrounds	17
6	Proposed experiment	20
7	Beam time request and summary	24
	References	26
8	Appendix A	28
8.1	Nuclear reaction mechanisms and their rates in stellar environments	28
8.2	The non-resonant reaction rate	30
8.3	The resonant reaction rate	31
8.4	The rate in the continuum	32

1 Introduction

1.1 The nucleosynthesis of fluorine

To date three different scenarios for the nucleosynthesis of fluorine have been proposed. The first includes the neutrino dissociation of ^{20}Ne in core collapse supernovae [1]. Goriely *et al.* [2] examined several possibilities including hydrostatic H- and He-burning, and explosive He-burning. They concluded that ^{19}F could be produced both during the thermal pulse phase of Asymptotic Giant Branch (AGB) stars and by hydrostatic burning in the He-shell of more massive stars. To date, none of the possibilities has been verified to dominate over the others. It is likely that all three contribute to the formation of fluorine in the universe.

1.2 Fluorine production in AGB stars

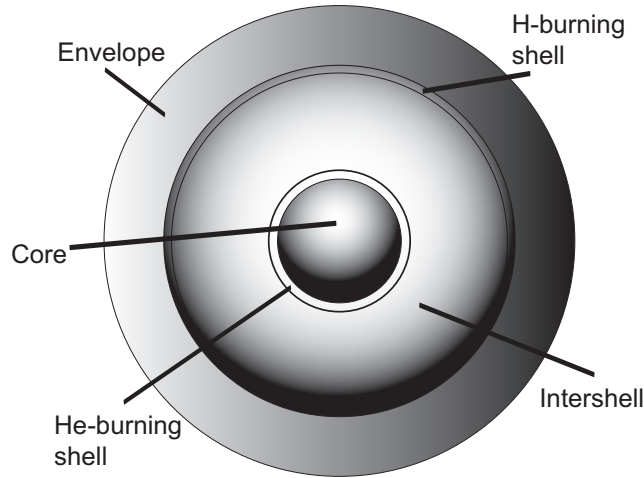


Fig. 1. Schematic of the structure of a star in the AGB phase. The core of the star is carbon and oxygen in an electron degenerate state. It is surrounded by a semiconvective He-rich intershell. The outer envelope of the star is convective and hydrogen rich. There are two thin regions where thermonuclear burning takes place simultaneously: an inner He-burning shell and a H-burning region below the convective envelope. The figure is not drawn to scale.

Fluorine nucleosynthesis in AGB stars takes place in the intershell region (see figure 1) when ^{14}N leftovers from the CNO cycle capture a ^4He from the He-rich environment. The unstable ^{18}F nucleus is formed and it decays with a half life of 109.8 minutes to ^{18}O . Both a proton or a ^4He can be captured by ^{18}O . In the former case an α -particle and a ^{15}N are

produced, while in the latter ^{22}Ne is made instead and “poisons” fluorine production. When ^{15}N captures an α -particle fluorine is produced. The environment in the intershell is not hydrogen rich so protons need to be produced in some way: the most efficient mechanism is the $^{14}\text{N}(n,p)^{14}\text{C}$ reaction. The neutrons required for this reaction to take place come from the $^{13}\text{C}(\alpha,n)^{16}\text{O}$ reaction. Some other protons may be mixed in when the convective envelope penetrates the intershell region at the end of the third dredge up (TDU) [3].

Mowlavi *et al.* [4] explained only the lowest fluorine overabundances observed at the surface of AGB stars. They proposed that an additional source of ^{13}C would account for the largest fluorine contents. Besides, they found that massive AGB stars will not produce large fluorine abundances and that low metallicity stars have less fluorine dredged-up to the surface than solar metallicity stars. However, the models they used did not reproduce the TDU consistently and they had to introduce it artificially [5].

One of the most important and interesting problems in AGB stellar structure and evolution is the formation of the ^{13}C -rich region that eventually would be the source of neutrons necessary not only for the synthesis of fluorine but for the main component of the s-process [6]. It is thought that ingestion of protons into the He intershell during the TDU leads to the formation of ^{13}C through the chain $^{12}\text{C}(p,\gamma)^{13}\text{N}(\beta^+\nu)^{13}\text{C}$, where ^{12}C is a product of He burning and therefore is relatively abundant in the intershell region [7]. However, the proton diffusion mechanism into the intershell is not well understood yet. Some possible explanations of the process include stellar rotation [8], convective overshooting [9], and gravitational waves [10].

With neutrons available in the environment an alternate reaction chain starting with the $^{14}\text{N}(n,p)^{14}\text{C}$ reaction is plausible as well. This reaction not only makes the protons required by $^{18}\text{O}(p,\alpha)^{15}\text{N}$ but also produces ^{14}C that may capture a ^4He and produce more of the ^{18}O required to synthesize fluorine.

Fluorine is very fragile. There are three main reactions that may lead to fluorine destruction. First, due to the high abundance of ^4He in the region, the $^{19}\text{F}(\alpha,p)^{22}\text{Ne}$ would play an important role. Second, other less abundant nuclei could be captured by fluorine as well. One case is protons via $^{19}\text{F}(p,\alpha)^{16}\text{O}$ and the other is neutrons with $^{19}\text{F}(n,\gamma)^{20}\text{F}$, where neutrons are produced by the $^{22}\text{Ne}(\alpha,n)^{25}\text{Mg}$ reaction.

The discovery of fluorine in extremely hot post-AGB stars with FUSE (Far Ultraviolet Spectroscopic Explorer) has been reported by Werner *et al.* [11]. Due to the high effective temperature of these stars material is usually highly ionized and absorption lines appear in the far ultraviolet region of the spectrum. The authors found very high overabundances of fluorine with respect to the solar abundance in hydrogen-deficient stars and confirmed the

general trend of increasing F abundance with increasing C abundance. Today, independent observations of overabundances of fluorine confirm that stars in the AGB phase are producers of this rare element. While fluorine overabundances measured are in good agreement with models of post AGB stars [12], the abundances obtained in models of AGB stars are very low compared to observations. A possible explanation could be a severe underestimation of the reaction rate of the $^{15}\text{N}(\alpha,\gamma)^{19}\text{F}$ process. Another possibility, the destruction mechanism $^{19}\text{F}(\alpha,p)^{22}\text{Ne}$ has been directly measured recently by [13]. The $^{18}\text{O}(p,\alpha)^{15}\text{N}$ process and the poison reaction $^{15}\text{N}(n,\gamma)^{16}\text{N}$ have also been studied indirectly with the trojan horse method by [14] at TAMU and by [15] at ORNL, respectively. None of these have been able to explain the present puzzle.

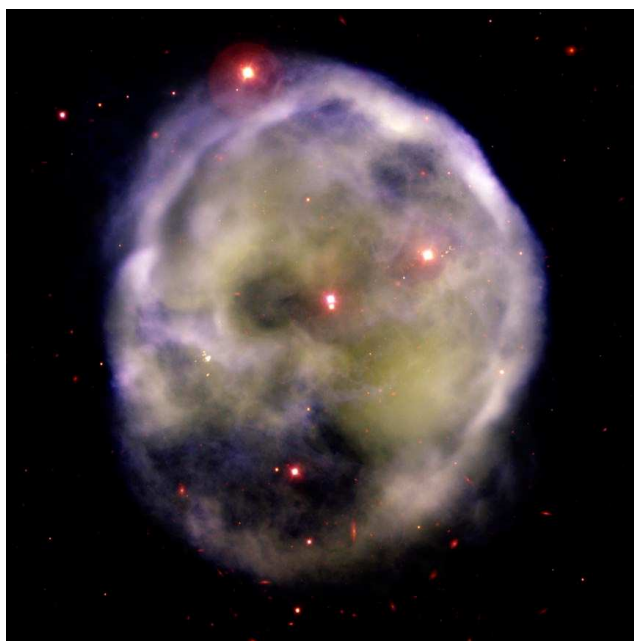


Fig. 2. Planetary nebula NGC 246. Fluorine has been identified in this PG1159 type object, now in the post AGB phase (as a white dwarf). Credit: Gemini South GMOS 2006.

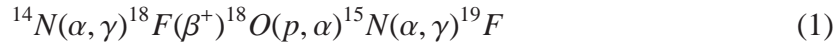
1.3 Fluorine production in Wolf-Rayet stars

The first quantitative work on nucleosynthesis of fluorine in hydrostatic He-burning sites was presented by [16]. They showed that it is not the He-burning shell that can produce fluorine but instead during the early He-burning core phase where the synthesis takes place. Nevertheless, they were concerned with the fact that the $^{19}\text{F}(\alpha,p)^{22}\text{Ne}$ reaction would have destroyed all fluorine by the end of that phase. The only way out of the problem was to

propose that the star would eject ^{19}F before the completion of the He-burning phase. The process of mass ejection while the core is burning He occurs in Wolf-Rayet stars; ^{19}F enrichment of the interstellar medium with fluorine can become important at higher metallicities.

Later on, [17] extended their own work by including a wider range of initial masses and metallicities in their analysis. They also included improved mass loss rates and a moderate core overshooting [18]. They concluded that the highest fluorine yields come from stars with solar metallicities and masses ranging between 40 and 85 M_{\odot} . Wolf-Rayet stars with lower metallicities have weaker winds and uncover the He-burning core only for the most massive stars but after ^{19}F has already been burned. For higher metallicities and for masses above 85 M_{\odot} , the H-burning core decreases so rapidly during the main sequence because of the strong stellar winds that the He-burning core becomes too small for being uncovered by the stellar winds later on.

Fluorine would be synthesized in Wolf-Rayet stars through the main reaction chain



where neutrons come from $^{13}\text{C}(\alpha, n)^{16}\text{O}$ and protons from $^{14}\text{N}(n, p)^{14}\text{C}$. The main source of fluorine destruction is thought to be $^{19}\text{F}(\alpha, p)^{22}\text{Ne}$. According to [17] Wolf-Rayet stars could account for most of the content of fluorine in the solar system. Nevertheless, fluorine has never been observed in a Wolf-Rayet star.

1.4 The current reaction rate of $^{15}\text{N}(\alpha, \gamma)^{19}\text{F}$

The thermonuclear reaction rate can be computed from a determination of the reaction cross section (see the appendix for a detailed description of the method). The cross section of this reaction is dominated by the contribution of three low energy resonances. The resonance strengths are based on the analysis of De Oliveira[19]. It should be noted though that there were several recent experimental studies which point towards a significantly higher reaction rate. De Oliveira et al.[20] themselves already suggested higher resonance strengths than given in their earlier paper. Direct α -capture measurements of the two higher energy states by Wilmes et al.[21] also indicate higher strengths. A recent indirect α -particle transfer analysis to the three resonance levels by [22] does suggest even higher values for the resonance strengths. Altogether the reaction rate of $^{15}\text{N}(\alpha, \gamma)^{19}\text{F}$ might be underestimated by a factor of five. Therefore, it is urgent to obtain a better determination of the rate for this reaction. The experiment proposed here intends to put closure to this problem.

2 Method

The new method is based on two principles: the reciprocity theorem for nuclear reactions, which relates the cross sections of forward and time-inverse nuclear processes, and the ability of a superheated liquid to induce nucleation when exposed to radiation [23]. Reciprocity allows one to deduce the cross section σ_A for particle capture (X, γ) processes to the ground state by measuring the cross section σ_B for photodisintegration (γ ,X) reactions, i.e.

$$\omega_A \frac{\sigma_A(X, \gamma)}{\lambda_\alpha^2} = \omega_B \frac{\sigma_B(\gamma, X)}{\lambda_\beta^2}, \quad (2)$$

where X is the captured particle, λ_α and λ_β are the channel wavelengths for capture and photodisintegration, and ω_A and ω_B are their respective spin factors. In the energy regimes discussed here, the transformation factor can provide a gain of over two orders of magnitude in cross section.

Capture reactions, such as (α , γ), (p, γ), and (n, γ), are responsible for many nucleosynthetic processes occurring in stellar environments. This is the case, for example, of the s process and the α process. Cases for which the reaction product is long lived can be studied experimentally by photodisintegration of the residual if a suitable target can be produced. When nuclei are photodisintegrated, the residual particles acquire an energy that adds up to the Q value of the reaction. If the energy of the γ ray is small compared to the mass of the target (this is the case for energies of relevance in astrophysics) the recoil energy is very small and for practical purposes it can be disregarded.

When a particle moves in a liquid, it deposits energy along its track until it is stopped. If enough energy is deposited in a short distance (linear density of energy deposition, or stopping power dE/dx), the liquid will be vaporized and a bubble will be formed. This is the “temperature spike” model of bubble formation [24]. Not all bubbles formed by this mechanism will eventually grow to become visible. In order to form a macroscopic bubble (a bubble visible to the unaided eye) enough energy E_c must be made available by the particle to form a bubble of critical radius

$$R_c = 2s/(P_v - P), \quad (3)$$

where P_v and P are the pressures of vapor and the liquid, respectively, and s is the surface tension of the liquid. The total energy and stopping power threshold conditions can be expressed as

$$\frac{dE}{dx} \geq \left(\frac{dE}{dx}\right)_c = \frac{E_c}{aR_c}, \quad (4)$$

and

$$E \geq E_c = \frac{4}{3}\pi R_c^3(\rho_v h + P) + 4\pi R_c^2\left(s - T\frac{\partial s}{\partial T}\right), \quad (5)$$

where ρ_v is the density of vapor, h is the enthalpy of vaporization, and T is the temperature of the liquid. The first term to the right is a volume term that accounts for the energy necessary to vaporize the liquid inside a bubble of radius R_c and the energy necessary to expand the bubble against the liquid pressure. The second term describes the energy necessary to form the bubble surface. Once the bubble has reached its critical size, as the liquid is superheated, the pressure of the gas inside the bubble will be larger than the pressure of the liquid around it and the bubble will continue growing unstopped. Vaporization of the whole volume of the liquid will occur unless the superheat is removed from the system. In practice this is done by a prompt pressurization of the liquid.

The process of preparation of this metastable state in liquids is shown in figure 3 for water. First, the liquid is pressurized at ambient temperature (1 to 2), then the pressure is kept constant while the temperature is increased to above the boiling point (2 to 3), and finally, the pressure is slowly released while keeping the temperature constant (3 to 4). At this point (4), water is still liquid but now superheated. It takes only a small disturbance to induce vaporization at this state. When this happens the bubble growth process needs to be controlled by increasing the liquid pressure (4 back to 3). It usually takes about one second for the liquid to return to a stable state (this depends mostly on the volume of the liquid being superheated and the maximum size reached by the bubble). Superheat is then returned into the system by releasing the pressure again (3 to 4), and the cycle is repeated for each bubble event in the detector.

The two threshold conditions from equations 4 and 5 are functions of the operating pressure and temperature of the liquid. Therefore, it is possible to tune the sensitivity of the detector to reject some minimum ionizing particles, while making it sensitive to heavy ions. Also, the detector is insensitive to the γ -ray beam at least at a level of one part in 1×10^9 [25]. However, there is one free parameter a in the theory. It relates the critical size bubble with the length L over which the particle transfers energy to the liquid by $L = aR_c$ [26]. This free parameter is a property of the liquid that needs to be determined by experimental means.

Figure 4 shows an example of stopping power curves for some ions in the liquid C_4F_{10} ,

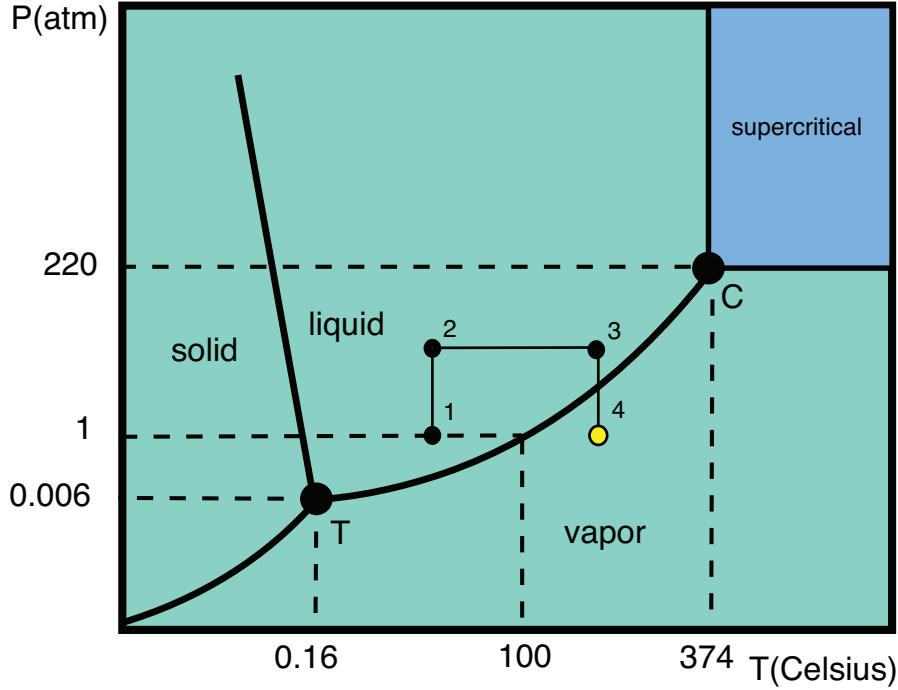


Fig. 3. Phase diagram for water. The path exemplifies the method for superheating a liquid and the operation (pressure and temperature cycle) of the bubble chamber.

as calculated with SRIM [27]. The energy loss for electrons, neutrons, and γ -rays is very small and does not appear in the plot. However, these particles may transfer their momentum to other ions by scattering interactions. For example, recoils from Compton scattering below 10 MeV do not have sufficient energy to trigger the bubble chamber. On the other hand, while insensitive to neutrons, bubble chambers can be triggered by them when they elastically scatter from the nuclei in the superheated liquid. While useful in the calibration of the detection thresholds, neutrons are also important background sources that need to be well understood in this kind of experiments. The dE/dx threshold condition for C_4F_{10} is very sharp, with a transition slope from no nucleation to full nucleation of only a few keV/cm, reaching a full nucleation efficiency of 100% [28].

We determined the free parameter in the theory by exposing the bubble chamber to a strong Pu/Be neutron source. By keeping the temperature of the liquid at a fixed value, the operating pressure was lowered from the saturation curve to a pressure at which the bubble chamber started triggering nucleation. This determined the (P,T) conditions at threshold.

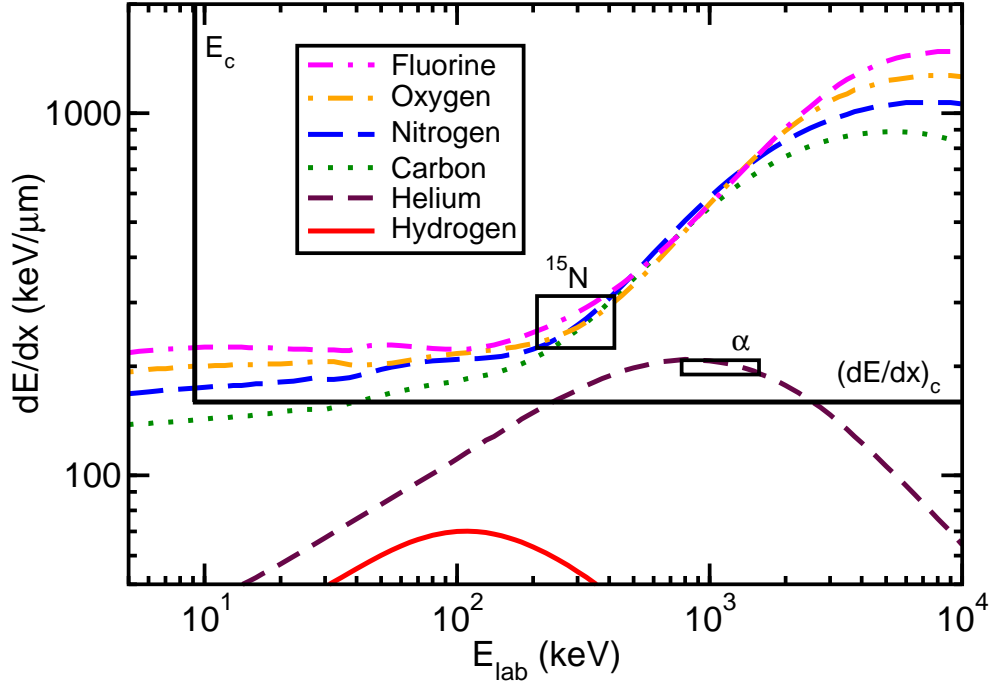


Fig. 4. (Color online). Thresholds for the liquid C_4F_{10} at $P = 193$ kPa and $T = 300$ K. The curves represent the stopping power of some ions relevant to C_4F_{10} as calculated with SRIM. The horizontal solid black line is the stopping power threshold. The energy threshold is represented by the solid vertical line at 9 keV. Particles above the horizontal threshold $(dE/dx)_c$ and to the right of the vertical E_c threshold will induce nucleation. The thresholds can be adjusted by changing the pressure and temperature conditions of the liquid, so some ion species can be discriminated while others detected. Moreover, the γ -ray beam passes through the detector without triggering bubble formation at all.

Meanwhile, given the energy spectrum of the neutrons it is assumed that the highest energy neutrons available will transfer the largest momentum to the ions in the liquid. This would happen for collisions in which neutrons are scattered at 180° . The heaviest ion species in the liquid will acquire the highest energy from the elastic scattering process. The energy E_{ion} is determined by kinematical considerations [29]

$$E_{ion} = \frac{1}{2}E_n(1 - \cos\theta)\left(1 - \left(\frac{A-1}{A+1}\right)^2\right), \quad (6)$$

where E_n is the neutron energy, θ is the scattering angle, A is the atomic mass of the ion in the liquid that scatters off the neutron.

Given the energy of the heaviest ion in the liquid, the corresponding value of dE/dx as predicted by SRIM will be the threshold value that enters equation 4. In the case of the liquid

C_4F_{10} , we determined the parameter to be $a=2.1\pm1.0$. This measurement is necessary to select the operating conditions of the liquid that would make it sensitive to some reactions, while rejecting some other sources of background.

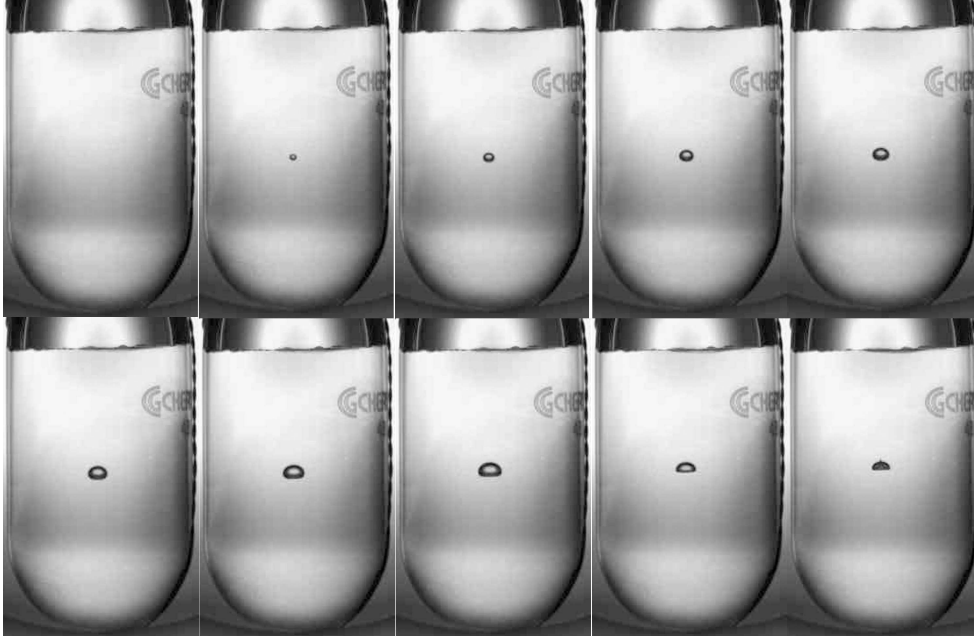


Fig. 5. Photograph sequence of an event registered by a 100 Hz video camera. The whole set spans 0.1 s, at equally spaced time intervals. The bubble was induced by ^{15}N from the $^{19}F(\gamma,\alpha)^{15}N$ reaction. Bubble detection is triggered by comparing the first two pictures in the sequence. Later on, at about 60 ms, the system responds by quenching the bubble until it disappears, about another 100 ms later.

3 Detector

The selection of the liquid to be used in the bubble chamber depends on several factors. Foremost, the molecular content of target ions whose photodisintegration cross section needs to be determined has to be maximized. Other ions present in the molecule of the liquid may be sources of background. Ideally, pure targets are desirable. However, either trace contaminants always exist, or the operating (P,T) conditions of the pure target in liquid form may be too extreme to work in a practical device. This is why usually the liquid of choice consists of more than one ion species. In principle, all liquids should nucleate in bubble chambers [30]. It is a matter of convenience to select materials that are liquid at normal pressure and temperature conditions.

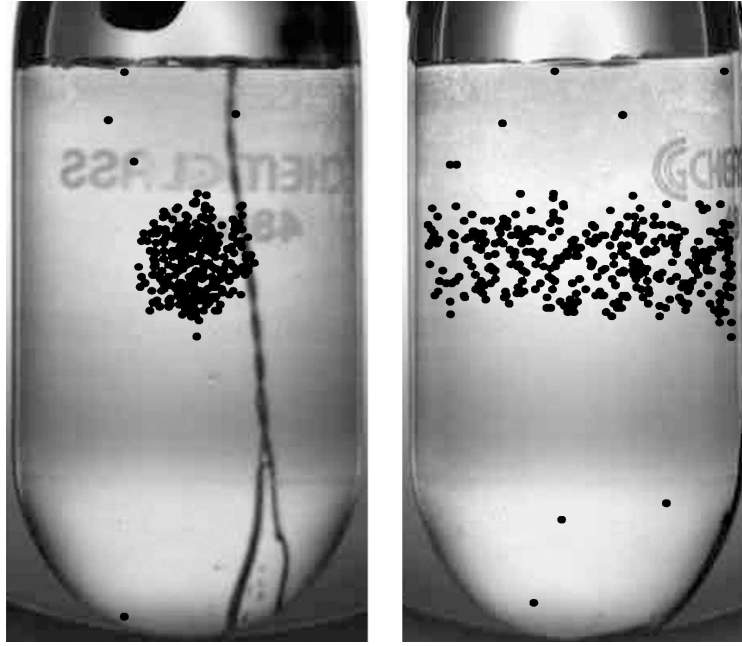


Fig. 6. Target vessel of the bubble chamber irradiated with a narrow band γ ray beam from HI γ S. Black dots show the sites of bubble formation for a γ -ray beam at energies between 8.7 and 10.0 MeV integrated over a period of 12 hours. The beam intensity was 4×10^3 γ /s and the liquid was the refrigerant R134a. Events outside of the beam region correspond to background from neutrons produced by cosmic rays and /or the walls of the experimental hall. The beam region contains photodisintegration events mainly from $^{19}\text{F}(\gamma, \alpha)^{15}\text{N}$ and an estimated 2% of cosmic ray induced background. The camera was placed at 45° relative to the beam direction.

Transparent liquids are also a convenient choice as optical imaging techniques can be applied to detect the bubble events and trigger the pressure system that stops bubble growth and vaporization of the whole liquid volume. This also requires the transparency of the vessel containing the superheated liquid, strongly constraining the material of choice seen by the beam before and after it reaches the sensitive liquid. Another promising technique for detecting bubble formation that does not have the transparency requirement is the detection of the sound produced by the fast and violent growth of the bubble in its early microscopic state. The disadvantage of this technique is that spatial resolution is well behind that of the optical method.

As opposed to conventional active gas targets frequently used in disintegration experiments, the liquids used in bubble chambers typically have densities a factor of 10^4 to 10^6 higher. This implies that the experimental yield obtained using a bubble chamber factors accordingly, considerably reducing the time the target needs to be exposed to the beam and making

the bubble chamber a device worth considering when measuring very small cross sections.

A nucleus photodisintegrated at several MeV γ -ray beam energies (of the kind of relevance to the type of experiments proposed here) will produce recoil products of some hundreds of keV to a few MeV in energy. This is very small compared to the high energy of particles that have been studied classically with bubble chambers. In those cases, particles leave behind bubble tracks that can be used to identify the nature of the events. However, the kind of experiments of interest here produce single bubble events that reflect the microscopic short range of the sources of nucleation (see figure 5).

The C_4F_{10} liquid is contained in a cylindrical glass vessel with a length of 10.2 cm and an outer diameter of 3.8 cm. Pictures of the superheated liquid are taken at 10 ms intervals by two CCD cameras mounted at 90° relative to each other. The images are then analyzed in real time by a computer and when a bubble is detected, the pressure in the glass vessel is increased within 40 ms of bubble formation from 54 kPa to 793 kPa. This leads to a quenching of the growing bubble thus preventing a boiling runaway of the liquid. The size of the bubbles is typically 1 to 2 mm in diameter after 40 ms. Their location is determined to a precision better than 1 mm. The spatial resolution is fundamental in the discrimination of some backgrounds, as discussed below.

4 Previous experiments

The concept for measuring cross sections for photon induced processes has been tested by exposing the bubble chamber to γ -rays produced with the HI γ S facility at Duke University [31]. The narrow bandwidth photon beam was generated by intracavity Compton backscattering of free-electron-laser light from high-energy electron beam bunches. This photon beam was collimated with a series of three, 10 cm long, copper cylinders that had a 1 cm circular hole and were aligned at 0° from the electron beam axis. The first collimator was located 52.8 m downstream from the collision point. We operated the storage ring in asymmetric two-bunch mode in order to reduce the beam energy spread.

The proof of principle of the technique was provided by comparing the count rate obtained in the detector while the γ -ray beam hit the superheated liquid against the count rate registered while no beam was produced by the accelerator. The spatial distribution of the events obtained from the cameras correlated very well with the 1 cm diameter size and position of the γ -ray beam (see figure 6).

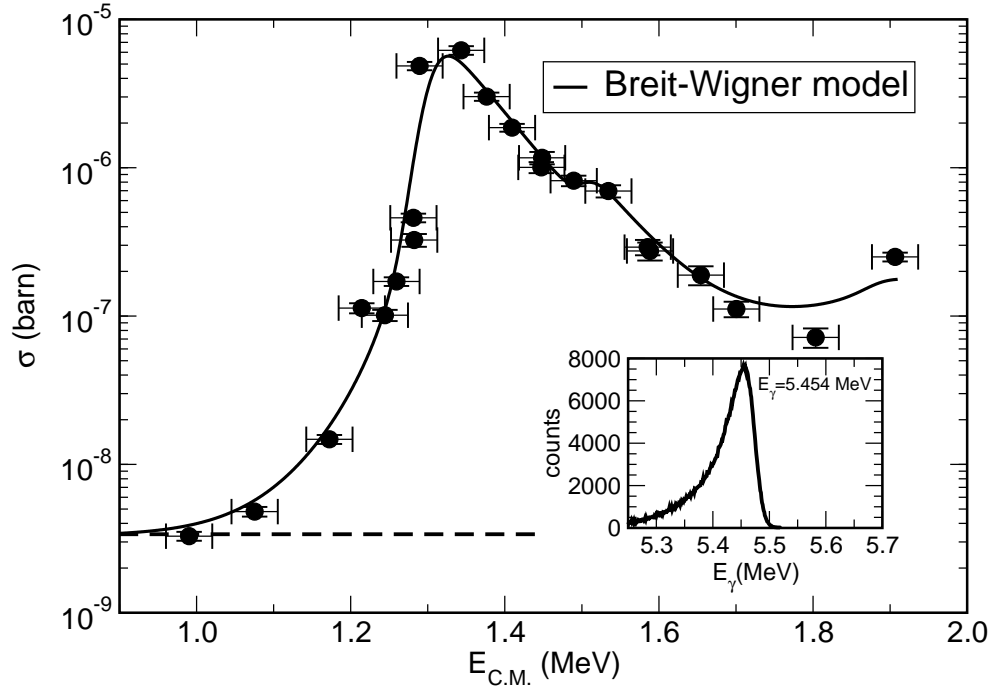


Fig. 7. Excitation function measured with a C_4F_{10} bubble chamber at $E_\gamma=5.0-6.0$ MeV ($E_{C.M.}=1.0-1.9$ MeV). The curve represents a model of the $^{15}N(\alpha,\gamma)^{19}F$ reaction convoluted with the γ -ray beam profile added to a bremsstrahlung induced background (also shown by the dashed line). The inset shows the profile of an example of HI γ S γ -ray beam (centroid at $E_\gamma = 5.454$ MeV) impinging on the bubble chamber.

Table 1

Nuclear parameters for the cross section model.

E_x (keV)	J^π	Γ (MeV)	Γ_α (MeV)	Γ_γ (MeV)	$\Gamma_{\gamma 0}$ (MeV)	$\Gamma_{\gamma 1}$ (MeV)	BR_0	$\omega\gamma$ (MeV)
4550	5/2+	1.01E-07	3.18E-11	1.01E-07	4.040E-09	9.696E-08	4	9.550E-11
4556	3/2-	3.87E-08	3.2E-12	3.87E-08	1.394E-08	2.478E-08	36	6.400E-12
5337	1/2+	1.3E-03	1.3E-03	1.690E-06	6.574E-07	1.033E-06	38.9	1.690E-06
5535	5/2+	4E-03	4E-03	1.147E-07	7.683E-09	1.070E-07	6.7	3.440E-07
5938	1/2+	8E-02	8E-02	4.16E-07	2.205E-08	3.940E-07	5.3	4.160E-07
6088	3/2-	4.7E-03	4.7E-03	2.5E-06	6.250E-07	1.875E-06	25	5.000E-06

The beam intensity was measured with a high-purity germanium detector placed downstream of the target. A thick aluminum absorber was placed between the bubble chamber and the γ -ray detector in order to limit the high photon flux incident on the detector crys-

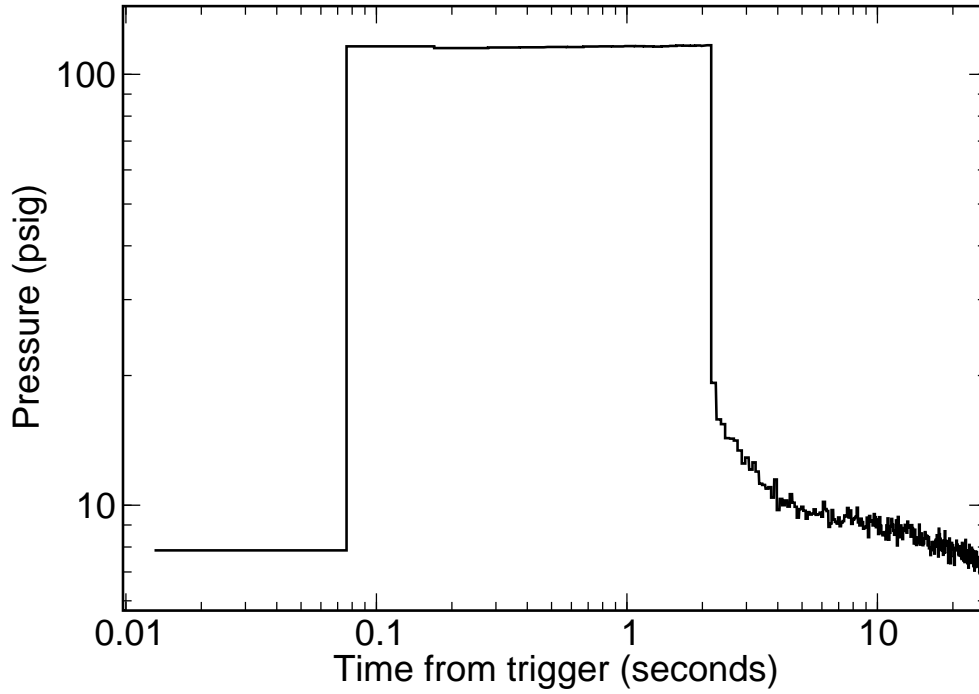


Fig. 8. Pressure profile of a bubble chamber cycle. The pressure in the glass vessel is increased within 40 ms of bubble formation from 54 kPa to 793 kPa. As the liquid becomes insensitive to charged particles when the superheat is removed by prompt compression, it is then left pressurized until the bubble is quenched. The system becomes thermodynamically stable and the release of the high pressure superheats the liquid again. The operating temperature averaged 37 °C.

tal. The γ -ray spectrum was then corrected with a Monte Carlo simulation of the response function of the detector and the attenuation in the absorber. The resulting spectrum then represents the γ -ray beam incident on the bubble chamber (see inset in figure 7). The beam intensity ranged from 2×10^3 γ/s to 3×10^6 γ/s , with a systematic error in its determination better than 5% [32]. The beam energy spread was kept below 2%.

The thickness of the liquid target was determined to be 3.0 ± 0.1 cm. The uncertainty was mainly determined by the position of the γ -ray beam with respect to the center of the target. This effect contributed a 3% systematic error in the determination of the measured cross sections.

The cross section obtained from the $^{19}\text{F}(\gamma, \alpha)^{15}\text{N}$ reaction converted to the $^{15}\text{N}(\alpha, \gamma)^{19}\text{F}$ scale using equation 2 is given by the points in figure 7. The thick solid line is the result of a calculation using the resonance parameters of the ^{19}F states in the $E_x=5-6$ MeV range obtained from the direct $^{15}\text{N}(\alpha, \gamma)^{19}\text{F}$ measurement of Ref. [21] (see table 1) and folding

Breit-Wigner resonances with the energy profile of the γ -ray spectrum (inset in figure 7). There is an excellent agreement between the results of the direct (α, γ) measurement and the time-inverse (γ, α) experiments. The cross section measured covers more than three orders of magnitude, ranging from about 3 nb to about 10 μb , with the point at the lowest energy corresponding to 242 counts accumulated in 35 minutes. Also, the excellent agreement between this experiment and previous work confirms the expectation that the bubble chamber is 100% efficient

The systematic error in the determination of the cross section was largely dominated by the dead time uncertainty of the bubble chamber. A dead time of two seconds was determined by sampling the pressure in the bubble chamber at a rate of 1 kHz after each event trigger. This pressure drop showed a gradual decline before the operating pressure and superheat were reached (see tail after decompression in figure 8). This decline was the main source of uncertainty in the dead time, found to be 0.9 seconds and introducing a systematic error in the range from $\pm 2\%$ up to $\pm 15\%$ for measurements at the highest count rate achieved. The count rate at the lowest cross section measured was typically 0.11 counts/s at an incident flux of 3×10^6 γ/s , demonstrating the high luminosity that has been achieved with the bubble chamber. The count rate tolerated by the bubble chamber ranges between 0.5 events per second down to 1 count per minute, or longer. In practice, this limit reflects the level of background obtained in the experiment.

5 Backgrounds

For the type of experiments discussed here, it is useful to define two different kinds of background sources that can contribute to the bubble count rate in the detector. The first contribution produces events that are spread evenly over the whole volume of the sensitive liquid. The second produces events that appear in the same spatial region as the γ -ray beam inside the superheated liquid. The first type can be determined in a straightforward manner by two independent methods: first, the count rate of events appearing outside of the beam region is compared to that of events in the path of the beam, while the γ -ray beam is irradiating the target. This is one of the reasons for which a good spatial resolution of the bubble chamber is required. In the experiment, this background contribution was determined to be about 8% of the count rate registered outside of the beam region. This value is in good agreement with the background observed in a second method, where the bubble chamber was moved to the side of the beam so that the liquid was not in the path of the γ rays. Sources of this background are fast neutrons produced by cosmic rays and by the photodisintegration of beamline and accelerator materials that are scattered into the

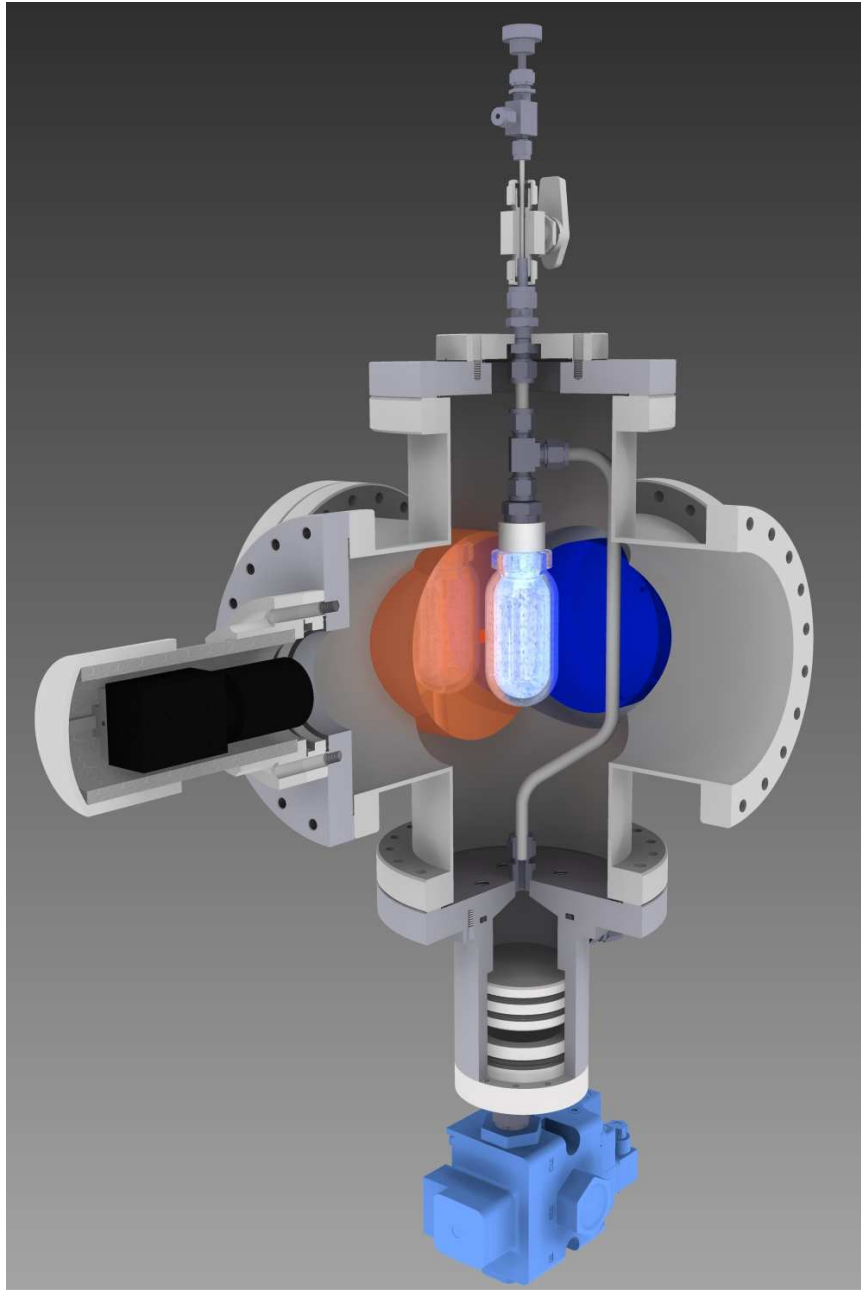


Fig. 9. The C₄F₁₀ bubble chamber detector enclosure for bremsstrahlung beams. The system is compact, so could fit easily in the tight space considered in this proposal

bubble chamber. This background contribution can be reduced by passively shielding the bubble chamber detector with a neutron absorbing material.

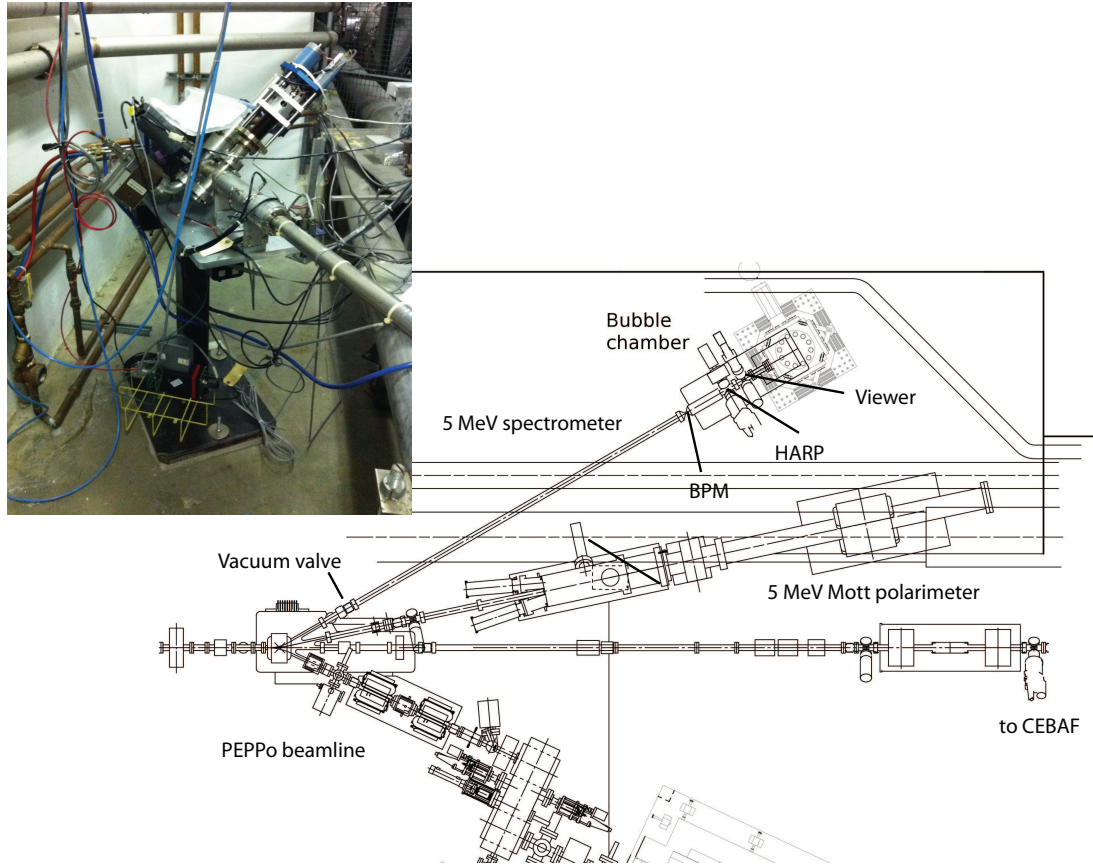


Fig. 10. Proposed location of the bubble chamber at the 5 MeV spectrometer beamline. Shown are a beam position monitor (BPM), a wire scanner (HARP) for measuring the beam size, and a viewer. Another BPM will be added on this beamline. There is a 1 kW beam dump at the end of the beamline. The beamline will be shortened in advance of the experiment. The photograph on the left shows the beamline.

The other background source cannot be easily corrected for by using the information from the fiducial volume. These background events are produced in the same spatial region as those from the photodisintegration reaction of interest. The main contributors to the count rate in this case are other reactions induced by neutrons produced upstream in the beam line and collimated in the same region as the γ -ray beam. This set of background sources can be suppressed by a) choosing the threshold conditions in the bubble chamber such that their interactions do not trigger bubble formation, b) by a subtraction of yields in which contaminant reactions are carefully accounted for, c) by placing a neutron absorber upstream in the beam line, and d) by identifying the neutrons from the sound they produce when inducing nucleation in the superheated liquid [33]. For example, this background source was studied in the HI γ S experiment by varying the flux of incident γ rays over two

Table 2

Integrated beam current requirements per data point as estimated with a Penfold-Leiss formalism. The statistical errors have been corrected to account for a cosmic ray background of 1 count/min and a background suppression factor of 10 from the bubble position information, as described in section 5.

Energy (MeV)	Q (μ A h)	events	statistical error (%)
4.55	400	348	8.3
4.65	100	633	4.3
4.75	30	709	4.0
4.85	10	824	3.6
4.95	3	813	3.6
5.05	1	864	3.5
5.15	.3	857	3.5
5.25	.1	1159	3.0
5.35	.01	1359	2.7

orders of magnitude at an energy of 5 MeV. At an incident flux of 3×10^6 γ /s the background allowed us to measure the cross section down to 3 nb. Most likely, the source of background was bremsstrahlung photons from the electron beam stored in the accelerator. Extrapolating to the highest flux that can be obtained at the HI γ S facility (1×10^8 γ /s), one expects to measure cross sections down to 200 pb. This is a considerable improvement over the 30 nb that have been measured from direct experiments where, below $E_{C.M.}=1.18$ MeV, only upper limits have been obtained [21].

6 Proposed experiment

The γ -ray beam at the HI γ S facility used for these experiments in the past is produced by a 0.5 GeV electron beam circulating in a storage ring. While the typical vacuum in the ring has values around 2×10^{-10} torr, this is enough to produce a bremsstrahlung γ ray component spanning from the electron beam energy down to the Compton backscattering energy and below. As the cross section for the $^{19}\text{F}(\gamma, \alpha)^{15}\text{N}$ reaction strongly depends on energy and within the bremsstrahlung high energies it is several orders of magnitude higher than

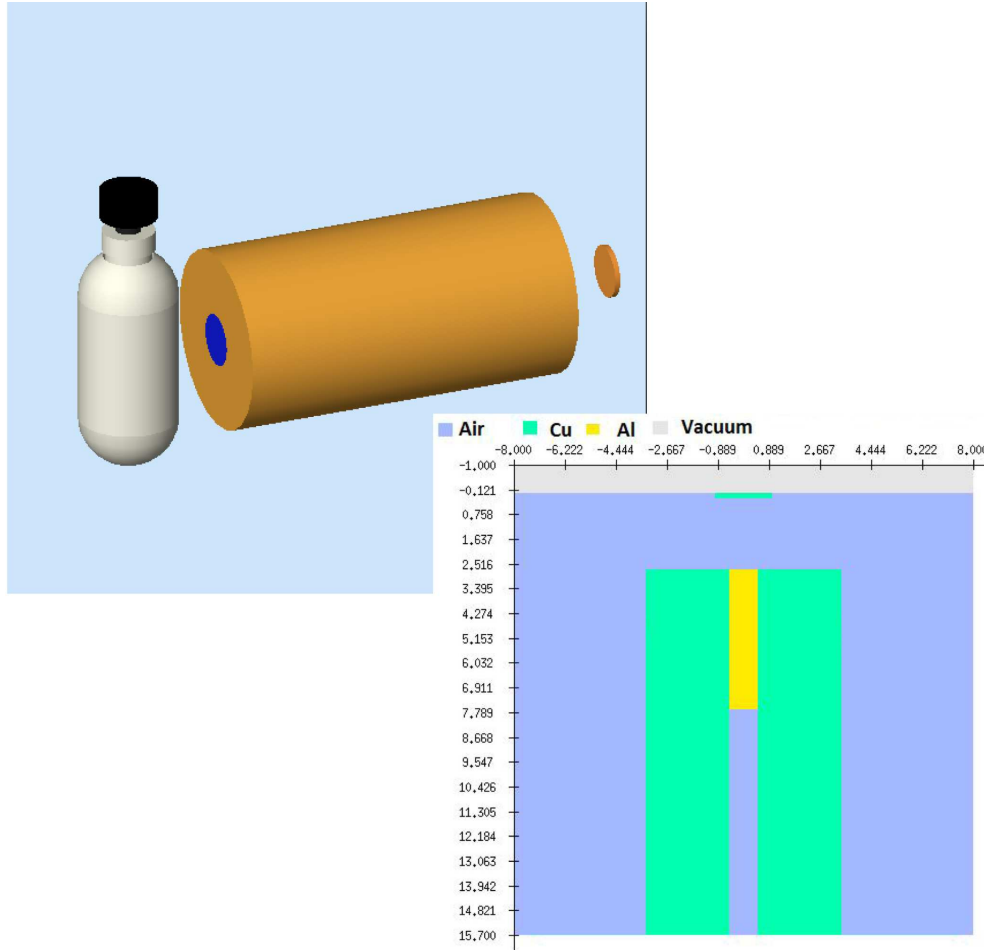


Fig. 11. Bremsstrahlung radiator and collimator assembly. The electron beam is incident on the device, first hitting a 2 mm thick Cu radiator (thin green line in lower figure). Further downstream, an Al (yellow) piece stops the remaining electron beam. This piece is supported by a cylindrical Cu collimator. The bubble chamber (upper figure) is then irradiated by the Bremsstrahlung photon beam produced by the radiator system.

the energy of interest, this becomes an important source of background that obscures the signal of interest. Therefore, by using the low energy electron beam produced by the injector at JLab incident on a bremsstrahlung radiator, this background will not be produced. The beam quality and infrastructure at JLab would be a perfect match for the bubble chamber experiments.

The bubble chamber enclosure has been redesigned to fit in the tight space of the 5 MeV spectrometer beam line. The system is light and compact and will allow for mounting an

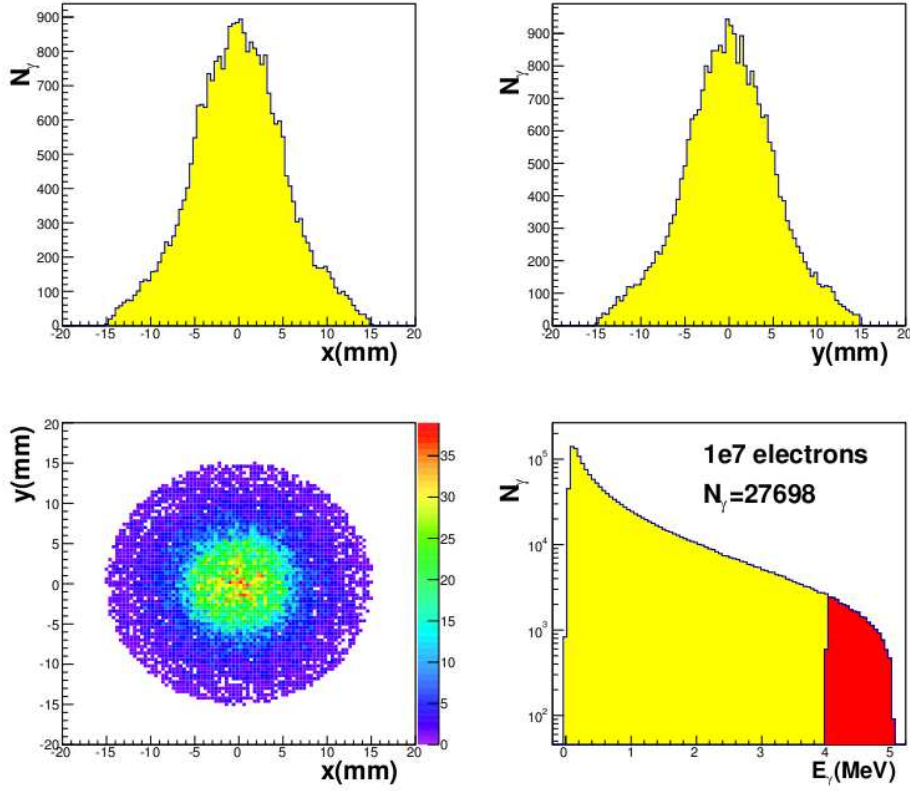


Fig. 12. Bremsstrahlung photon beam profiles for a 10 mm diameter collimator and 2 mm thick Cu radiator exposed to a 5 MeV electron beam as computed with a Monte Carlo simulation.

aluminum beam dump behind the bubble chamber. The enclosure (see figure 9) will allow for safe operation of the device and has surpassed all safety standards required by Argonne National Laboratory. The location of the bubble chamber in the injector tunnel is shown in figure 10.

We propose to test this scheme in a first experiment measuring the $^{19}\text{F}(\gamma, \alpha)^{15}\text{N}$ reaction at energies between 4.6 and 5.4 MeV. The γ ray beam will be produced by irradiating a Cu radiator (see figure 11) with the electron beam. A calculation of the expected γ ray beam profiles has been obtained with a Monte Carlo simulation of the electron beam impinging on the collimator-radiator system. The expected γ ray beam profiles are shown in figure 12.

While the injector is able to provide higher beam intensities, a conservative limit of $20 \mu\text{A}$ of beam current due to the Cu radiator has been established for this experiment. This will be enough to study the cross section down to value of about $1 \times 10^{-35} \text{ cm}^2$ (see figure 14).

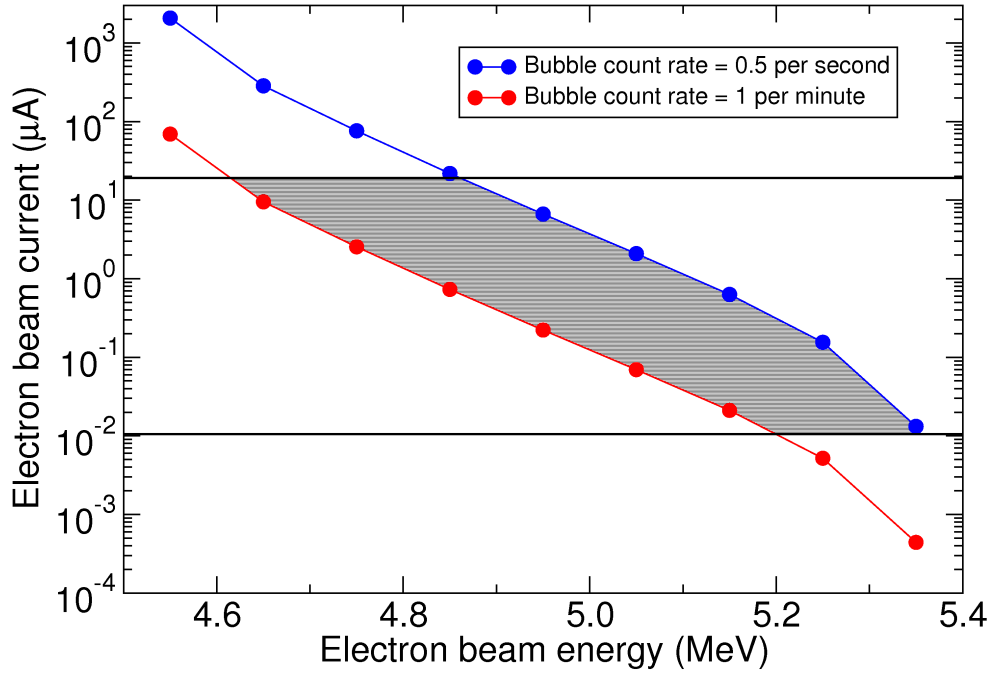


Fig. 13. Beam parameter space available to the proposed experiment (region in gray). The horizontal solid lines delimit the beam current operation regime of the injector. The blue curve corresponds to the photodisintegration yield as computed by assuming a maximum bubble count rate of 0.5 Hz. The red curve assumed a minimum rate of one count per minute, primarily determined by background events.

Improved heat dissipation in the radiator would allow us to increase the beam intensity in the future. The estimates of the integrated beam current required to perform the experiment (see table 2) were performed by deconvoluting the beam profile from the experimental yield by means of the Penfold-Leiss method [34] [35]. The count rates tolerated by the bubble chamber were assumed to be between 0.5 Hz and 0.016 Hz. Assuming a maximum electron beam current of $20 \mu\text{A}$ and 10 nA a lower limit for measuring its intensity with the available beam current monitors at JLab, the beam parameter space where these experiments could operate is shown in figure 13. The bubble chamber operating conditions will be the same as in the HI γ S experiment, shown in figure 8.

The main source of background is expected to be cosmic ray induced neutrons. This rate is expected to be close to one per minute, consistent with that measured at HI γ S and ANL, where there is a similar overburden of shielding. Since we plan to operate this experiment during nights and weekends to avoid any conflict with the ongoing 12 GeV upgrade activities, we will measure this cosmic background during the day when the beam is off.

If the beam induced background is indeed small, we will propose to study in a second set of experiments the $^{19}\text{F}(\gamma, \alpha)^{15}\text{N}$ and $^{16}\text{O}(\gamma, \alpha)^{12}\text{C}$ reactions at lower energies. In particular, there is an astrophysically important resonance in $^{19}\text{F}(\gamma, \alpha)^{15}\text{N}$ at $E_\gamma = 4.38$ MeV. It could be possible that the main mechanism of fluorine nucleosynthesis in the universe proceeds via this resonance.

7 Beam time request and summary

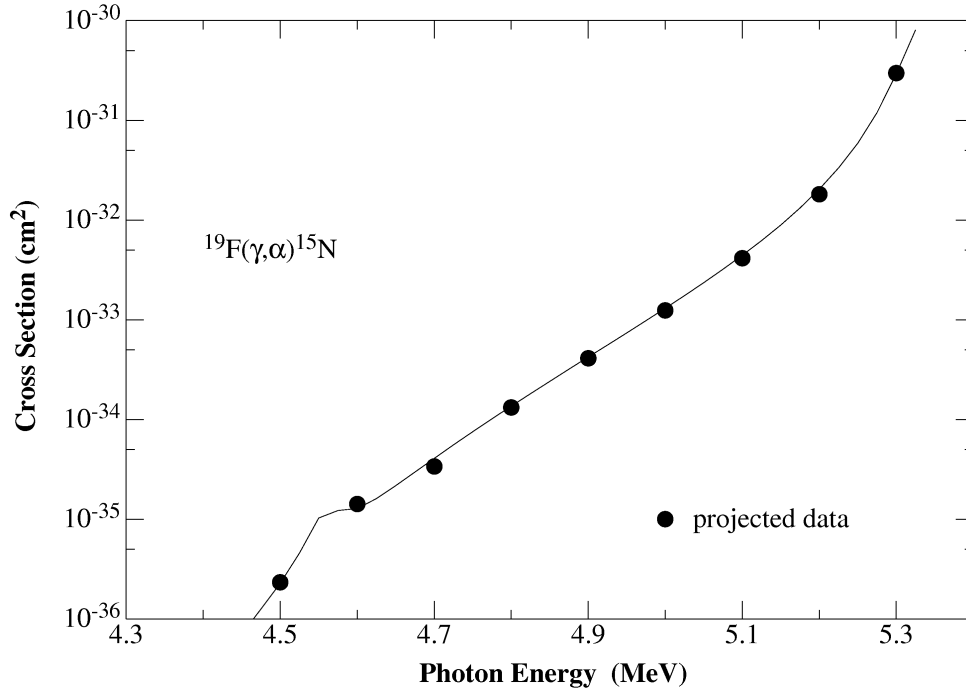


Fig. 14. Expected cross section measurements from this experiment.

We have provided a proof of principle of the operation of the bubble chamber as a low rate counter for photodisintegration events, including the determination of the $^{15}\text{N}(\alpha, \gamma)^{19}\text{F}$ reaction with a narrow band γ -ray beam impinging on a ^{19}F target. The use of bremsstrahlung for this type of measurements will be explored at JLab. The main challenge in the whole experimental program is the careful and systematic characterization of the various sources of

Table 3

Electron beam time needed for the experiment.

	Energy (MeV)	Beam current (μA)	count rate (1/s)	beam time (h)
Experiment	4.55	2.0E+01	1.6E-02	20.0
	4.65	1.3E+01	2.4E-02	7.5
	4.75	5.0E+00	3.3E-02	6.0
	4.85	1.7E+00	3.9E-02	5.8
	4.95	6.5E-01	4.9E-02	4.6
	5.05	2.4E-01	5.8E-02	4.2
	5.15	8.4E-02	6.7E-02	3.6
	5.25	3.0E-02	9.7E-02	3.3
	5.35	1.0E-02	3.8E-01	1.0
Beam energy change				16.0
Checkout				8.0
Commissioning				20.0
Total				100.0

background. For this we have redesigned the bubble chamber and we will use superheated perfluorobutane (C_4F_{10}) as a sensitive liquid. Upon success of the proposed experiment, we will submit another proposal for measuring the $^{12}\text{C}(\alpha, \gamma)^{16}\text{O}$ reaction rate with a water bubble chamber.

A total of 100 hours of beam time are requested. The time budget comprises 56 hours of beam time (100% efficiency of experiment and accelerator beam-on-target time) for the measurements (see table 3), plus two hours per energy change for beam tuning. Eight hours of check out beam time will be needed. These will include placing a neutron absorber before the beam hits the detector. As the bubble chamber will be exposed to a bremsstrahlung beam for the first time, an additional 20 hours of beam time will be required to commission the device. Here we will study the detector response to changes in the beam parameters and verify that background rates are similar to the expected values. In total, this amounts to 100 hours of beam time.

References

- [1] S. E. Woosley and W. C. Haxton. Supernova neutrinos, neutral currents and the origin of fluorine. Nature, 334:45–47, 1988.
- [2] S. Goriely, A. Jorissen, and M. Arnould. On the mechanisms of ^{19}F production. Max-Planck-Institut für Physik und Astrophysik Rep., 1989.
- [3] A. I. Karakas. Asymptotic Giant Branch Stars: their influence on binary systems and the interstellar medium. PhD thesis, Monash University, 2003.
- [4] N. Mowlavi, A. Jorissen, and M. Arnould. Fluorine production in intermediate-mass stars. Astron. Astrophys., 311:803, 1996.
- [5] M. Forestini, S. Goriely, A. Jorissen, and M. Arnould. Fluorine production in thermal pulses on the asymptotic giant branch. Astron. Astrophys., 261:157–163, 1992.
- [6] M. Busso, R. Gallino, and G.J. Wasserburg. Nucleosynthesis in asymptotic giant branch stars: relevance for galactic enrichment and solar system formation. Ann. Rev. Astron. Astrophys., 37:239–309, 1999.
- [7] I. Iben Jr. and A. Renzini. On the formation of carbon star characteristics and the production of neutron-rich isotopes in asymptotic giant branch stars of small core mass. Ap. J., 263:L23–L27, 1982.
- [8] N. Langer, A. Heger, S. Wellstein, and F. Herwig. Mixing and nucleosynthesis in rotating TP-AGB stars. Astron. Astrophys., 346:L37–L40, 1999.
- [9] F. Herwig, T. Blöcker, D. Schönberner, and M. El Eid. Stellar evolution of low and intermediate-mass stars. IV. Hydrodynamically-based overshoot and nucleosynthesis in AGB stars. Astron. Astrophys., 324:L81–L84, 1997.
- [10] P. A. Denissenkov and C. A. Tout. Partial mixing and formation of the ^{13}C pocket by internal gravity waves in asymptotic giant branch stars. Mon. Not. R. Astron. Soc., 340:722–732, 2003.
- [11] K. Werner, T. Rauch, and J. W. Kruk. Fluorine in extremely hot post-AGB stars: Evidence for nucleosynthesis. Astron. Astrophys., 433:641–645, 2005.
- [12] M. Lugaro, C. Ugalde, A. I. Karakas, M. Wiescher, J. Görres, J. C. Lattanzio, and R. C. Cannon. Reaction rates uncertainties and the production of ^{19}F in AGB stars. Ap. J., 615:934–946, 2004.
- [13] C. Ugalde et al. The thermonuclear rate for the $^{19}\text{F}(\alpha, p)^{22}\text{Ne}$ reaction at stellar temperatures. Phys. Rev. C, 77:035801, 2008.
- [14] M. La Cognata *et al.* Effect of high energy resonances on the $^{18}\text{O}(p, \alpha)^{15}\text{N}$ reaction rate at agb and post agb relevant temperatures. Ap. J., 723:1512, 2010.

- [15] D. W. Bardayan *et al.* Spectroscopic study of low lying ^{16}N levels. Phys. Rev. C, 78:052801(R), 2008.
- [16] G. Meynet and M. Arnould. Synthesis of ^{19}F in the He-Burning Zones of Massive Stars. IOP, Bristol, 1993.
- [17] G. Meynet and M. Arnould. Synthesis of ^{19}F in Wolf-Rayet stars. Astron. Astrophys., 355:176–180, 2000.
- [18] G. Meynet, A. Maeder, G. Schaller, D. Schaerer, and C. Charbonnel. Grids of massive stars with high mass loss rates. V. from 12 to $120 M_{\odot}$ at $z = 0.001, 0.004, 0.008, 0.020$, and 0.040 . Astron. Astrophys. Sup., 103:97–105, 1994.
- [19] F. de Oliveira. Determination of α -widths in ^{19}F relevant to fluorine nucleosynthesis. Nucl. Phys. A, 597:231–252, 1996.
- [20] F. de Oliveira. Comparison of low-energy resonances in $^{15}\text{N}(\alpha, \gamma)^{19}\text{F}$ and $^{15}\text{O}(\alpha, \gamma)^{19}\text{Ne}$ and related uncertainties. Phys. Rev. C, 55:3149–3151, 1997.
- [21] S. Wilmes, V. Wilmes, G. Staudt, P. Mohr, and J.W. Hammer. The $^{15}\text{N}(\alpha, \gamma)^{19}\text{F}$ reaction and nucleosynthesis of ^{19}F . Phys. Rev. C, 66:065802, 2002.
- [22] H.T. Fortune and A.G. Lacaze. Reliability of α strengths for weak states. Phys. Rev. C, 67:064305, 2003.
- [23] D. A. Glaser. Some effects of ionizing radiation on the formation of bubbles in liquids. Phys. Rev., 87:665, 1952.
- [24] F. Seitz. On the theory of the bubble chamber. Phys. Fluids, 1:2, 1958.
- [25] W. J. Bolte *et al.* Development of bubble chambers with enhanced stability and sensitivity to low energy nuclear recoils. Nucl. Instr. and Meth. A, 577:569–573, 2007.
- [26] M. J. Harper. Calculation of recoil ion effective track lengths in neutron-radiation-induced nucleation. Nucl. Sci. Eng., 114:118–123, 1993.
- [27] J. F. Ziegler, J. P. Biersack, and U. Littmark. The Stopping and Range of Ions in Solids. Pergamon Press, 2009.
- [28] V. Zacek. Search for dark matter with moderately superheated liquids. Nuovo Cimento A, 107:291–298, 1994.
- [29] S. Glasstone and M. C. Edlund. The elements of nuclear reactor theory. Van-Nostrand, 1952.
- [30] D. A. Glaser. Elementary Particles and Bubble Chambers. Elsevier Publishing Company, Amsterdam, 1964.

- [31] H. R. Weller *et al.* Research opportunities at the upgraded HI γ S facility. Prog. Part. Nucl. Phys., 62:257, 2009.
- [32] S. Carson *et al.* Ratio of germanium detector peak efficiencies at photon energies of 4.4 and 11.7 mev: Experiment versus simulation. Nucl. Instr. and Meth. A, 618(1-3):190 – 198, 2010.
- [33] F. Aubin *et al.* Discrimination of nuclear recoils from alpha particles with superheated liquids. New J. Phys., 10:103117, 2008.
- [34] A. S. Penfold and J. E. Leiss. Analysis of photonuclear cross sections. Phys. Rev., 114:1332, 1959.
- [35] D. J. S. Findlay. A modification to the Penfold-Leiss method of cross section unfolding. Nucl. Instr. and Meth., 213:353, 1983.
- [36] R. V. Wagoner. Synthesis of the elements within objects exploding from very high temperatures. Ap. J. Suppl., 18(162):247–295, 1969.
- [37] T. Rauscher, F.K. Thielemann, and K.L. Kratz. Nuclear level density and the determination of thermonuclear rates for astrophysics. Phys. Rev. C, 56:1613–1625, 1997.
- [38] G. Gamow. Z. Phys, 51:204, 1928.
- [39] C. Rolfs. private communication, 2002.

8 Appendix A

8.1 Nuclear reaction mechanisms and their rates in stellar environments

The relevant quantity entering the computation of the stellar structure and nucleosynthesis that quantifies the probability of a thermonuclear reaction is the reaction rate per pair of particles $\langle\sigma v\rangle$. For a gas of particles a with a density N_a and particles b with a density N_b , the reaction rate per unit volume r is the product of σN_b with the flux of particles a vN_a . Here σ is the reaction cross section of particles a and b and v is their relative velocity, i.e.

$$r = N_a N_b v \sigma. \quad (7)$$

The relative velocity of particles in a gas is described by a distribution so the rate needs to be averaged over v . In general the reaction cross section is energy dependent, so we write

$$r = N_a N_b \langle v \sigma(v) \rangle, \quad (8)$$

such that

$$\langle v\sigma(v) \rangle = \int_0^\infty \sigma(v)\phi(v)v dv. \quad (9)$$

For the special case of a threshold for the reaction at positive energies the lower limit of the integral is replaced by the velocity at threshold. The velocities in stellar AGB and Wolf-Rayet environments are described by a non degenerate gas with a Maxwell-Boltzmann distribution, and with $E = mv^2/2$, we write the expression for the rate as

$$\langle v\sigma(v) \rangle = \left(\frac{8}{\pi\mu}\right)^{1/2} (kT)^{-3/2} \int_0^\infty \sigma(E)E \exp\left(-\frac{E}{kT}\right) dE, \quad (10)$$

such that k is Boltzmann's constant and μ is the reduced mass.

The cross section measurement (or theoretical prediction, in the worst case scenario) involves a good part of work efforts in nuclear astrophysics. Approximations to the reaction rate are very useful, though. For example, relative to the energy dependence of the cross section the reaction rate can be of three different types [36], i.e.

$$\langle v\sigma(v) \rangle = \langle v\sigma(v) \rangle_{nr} + \langle v\sigma(v) \rangle_r + \langle v\sigma(v) \rangle_c, \quad (11)$$

such that “nr” labels the non-resonant part of the rate; it dominates at the lowest energies, where it is not likely to find resonances in the cross section. The term $\langle v\sigma(v) \rangle_r$ is the resonant part of the rate and in this region the cross section shows well isolated resonances. Finally, $\langle v\sigma(v) \rangle_c$ stands for the continuum term, where the density of resonances per energy interval D is high ($D > 10 \text{ MeV}^{-1}$ [37]).

For the case of a reaction between two charged particles, one of the reasons the determination of the cross section at stellar temperatures is an interesting problem is the fact that Coulomb repulsion is extremely strong. Nuclear reactions do not happen frequently, so the values of the cross section that are involved are in general too small to be measured in the laboratory.

The energy dependence of the cross section was examined for the case of α -particle decay [38], who found that the probability P that a pair of charged particles would overcome the Coulomb barrier can be written as

$$P \sim \exp(-2\pi\eta) \sim \exp(-(E_G/E)^{1/2}), \quad (12)$$

with

$$\eta = \frac{Z_1 Z_2 e^2}{\hbar v}, \quad (13)$$

$$E_G = 2\mu(\pi\eta v)^2, \quad (14)$$

Z_1 and Z_2 the atomic numbers of the particles, \hbar the reduced Planck constant, v the relative velocity of the particles, and e the proton charge. On the other hand, the cross section should be proportional to the effective geometrical area $\pi\lambda^2$ seen by the particle pair during the collision, such that

$$\sigma \sim \pi\lambda^2 \sim \left(\frac{1}{p}\right)^2 \sim \left(\frac{1}{E}\right) \quad (15)$$

where p is the linear momentum and λ the de Broglie wavelength. In this way we may write

$$\sigma(E) = \frac{S(E)}{E} \exp(-2\pi\eta), \quad (16)$$

with $S(E)$ known as the astrophysical S-factor. By substituting equation 16 into equation 10 we finally get

$$\langle\sigma v\rangle = \left(\frac{8}{\pi\mu}\right)^{1/2} (kT)^{-3/2} \int_0^\infty S(E) \exp\left(-\frac{E}{kT} - \frac{b}{E^{1/2}}\right) dE. \quad (17)$$

Writing the cross section as in equation 16 is just a matter of convenience as the S-factor has no physical meaning [39]; nevertheless it is very useful in removing the strong energy dependence of the cross section—usually spanning several orders of magnitude in a small energy region— thus enhancing the visualization of the resonant nature of the reaction.

8.2 The non-resonant reaction rate

In general $S(E)$ can be written as a Taylor series around an energy E_0 ; in the special case of a non-resonant reaction $S(E)$ is a constant given by $S_0 = S(E_0)$. Taking S_0 out of the integral in equation 17 the reaction rate per particle pair concept can be put in a more practical context for stellar astrophysics. The first factor in the integrand of equation 17 represents the probability density that two particles would collide with each other at an energy E , and is given by a Maxwell-Boltzmann distribution. On the other hand the second factor in the integrand gives the probability that once a pair of particles have encountered each other at an energy E they would penetrate the Coulomb barrier and be thrown into a reaction channel. The product of the integrands defines a region of energy where given a gas with temperature $E = kT$ the reactions between particles a and b are likely to take place. The region is known as the "Gamow window".

The concept of the Gamow window can be extended to reaction regimes different from the non-resonant mechanisms by assuming $S(E) = S_0$. In this way the relevance of a cross

section in an astrophysical environment can be assessed before solving and evolving the set of equations for stellar structure and evolution.

8.3 The resonant reaction rate

For the case of an isolated sharp resonance, the cross section can be written as

$$\sigma(E) = \frac{\lambda^2}{4\pi} \frac{2J+1}{(2I_1+1)(2I_2+1)} \frac{\Gamma_{in}\Gamma_{out}}{(E-E_R)^2 - (\Gamma/2)^2}, \quad (18)$$

where λ is the de Broglie wavelength, E_R is the energy of the resonance J is the spin of the compound state, I_1 and I_2 are the spins of the colliding nuclei, Γ_{in} and Γ_{out} are the partial widths for the entrance and exit channel, respectively, and Γ is the total width. The total width Γ is defined as the sum of the partial widths

$$\Gamma = \sum_i \Gamma_i, \quad (19)$$

and

$$\Gamma\tau = \hbar, \quad (20)$$

where τ is the lifetime of the state at E_R . On the other hand the partial widths Γ_i are a product of the penetration factor P and the squared matrix element γ of the transition between the channel and the compound state, i.e.

$$\Gamma_i = 2P\gamma^2. \quad (21)$$

Substituting in equation 10

$$\langle\sigma v\rangle = \left(\frac{8}{\pi\mu}\right)^{1/2} (kT)^{-3/2} \int_0^\infty \frac{\lambda^2}{4\pi} \omega \frac{\Gamma_{in}\Gamma_{out}}{(E-E_R)^2 - (\Gamma/2)^2} E \exp\left(-\frac{E}{kT}\right) dE, \quad (22)$$

where the spin factor ω is defined as

$$\omega = \frac{2J+1}{(2I_1+1)(2I_2+1)}. \quad (23)$$

Assuming $E \exp(-E/kT)$ changes very little in the resonance region we can write

$$\langle\sigma v\rangle = \left(\frac{8}{\pi\mu}\right)^{1/2} \frac{\lambda^2}{4\pi} \omega E_R \frac{\Gamma_{in}\Gamma_{out}}{(kT)^{3/2}} \exp\left(-\frac{E_R}{kT}\right) \int_0^\infty \frac{dE}{(E-E_R)^2 - (\Gamma/2)^2}, \quad (24)$$

such that the integral evaluates to $2\pi/\Gamma$. Let us define $\gamma = \Gamma_{in}\Gamma_{out}/\Gamma$, so

$$\langle\sigma v\rangle = \omega\gamma\left(\frac{2\pi}{\mu kT}\right)^{3/2} \hbar^2 \exp\left(-\frac{E_R}{kT}\right). \quad (25)$$

The case of several resonances can be approximated by summing over various terms of the form (25), i.e.

$$\langle\sigma v\rangle_R = \left(\frac{2\pi}{\mu kT}\right)^{3/2} \hbar^2 \sum_i (\omega\gamma)_i \exp\left(-\frac{E_R}{kT}\right)_i. \quad (26)$$

The rate described in this proposal is calculated using the expression for $\langle\sigma v\rangle_R$ given above.

8.4 The rate in the continuum

At energies where the density of states is high ($D > \Gamma$) the sum over resonances can be approximated by an integral over E_R [36]. The rate is then obtained by retaining the most energy-dependent terms. The rate in the continuum can still be written as a sum of two terms:

$$\langle\sigma v\rangle_c = \langle\sigma v\rangle_{uc} + \langle\sigma v\rangle_{sc}. \quad (27)$$

The first term corresponds to the “unsaturated continuum” rate and here the entrance channel partial width Γ_{in} is small compared to the total width Γ . The second term is the “saturated continuum” term, where the penetration factor (equation 12) is large enough to allow the incoming partial width approximate Γ , the total width. In general the functional dependence of the continuum rates with energy is as follows:

$$\langle\sigma v\rangle_{uc} = FT_9^{-2/3} \exp[-\tau_c T_9^{-1/3} - (T_9/T_u)^2] \quad (28)$$

and

$$\langle\sigma v\rangle_{sc} = H \exp[-11.605E_c/T_9], \quad (29)$$

such that T_9 is the temperature in GK, and E_c , F , H , τ_c , and T_u are constants.